



Enhanced grain-boundary conduction in polycrystalline $\text{Ce}_{0.8}\text{Gd}_{0.2}\text{O}_{1.9}$ by zinc oxide doping: Scavenging of resistive impurities

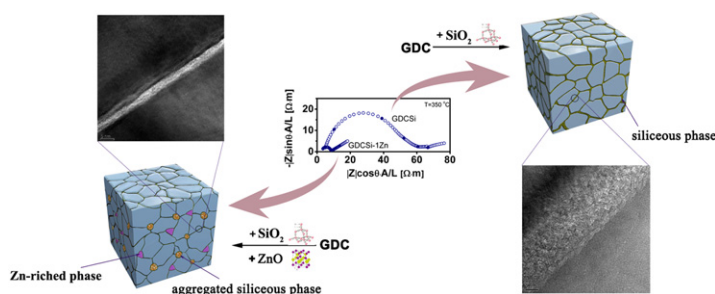
Lin Ge, Ruifeng Li, Shoucheng He, Han Chen, Lucun Guo*

College of Materials Science and Engineering, Nanjing University of Technology, No. 5 Xinmofan Road, Nanjing, Jiangsu, 210009, PR China

HIGHLIGHTS

- ▶ ZnO doping can diminish the deleterious effect caused by impurities on GDC.
- ▶ TEM-EDS analysis reveals a novel scavenging mechanism.
- ▶ A 3D schematic is established to elucidate the role of ZnO in the CeO_2 – Gd_2O_3 system.

GRAPHICAL ABSTRACT



ARTICLE INFO

Article history:

Received 18 October 2012

Received in revised form

7 December 2012

Accepted 13 December 2012

Available online 27 December 2012

Keywords:

Doped ceria

Grain-boundary conduction

Scavenging mechanism

Solid oxide fuel cells

ABSTRACT

ZnO doping can significantly diminish the deleterious effect caused by impurities on the grain-boundary conduction of polycrystalline $\text{Ce}_{0.8}\text{Gd}_{0.2}\text{O}_{1.9}$ electrolyte. Analysis by field emission transmission electron microscopy equipped with energy-dispersive X-ray spectroscopy reveals that the siliceous and ZnO phases are separately aggregated at the triple grain junction areas in ZnO-added specimens. This finding implies that the scavenging process does not occur via the expected formation of zinc silicates, but via a novel mechanism in which resistive siliceous phases strongly aggregate in non-wetting configurations induced by ZnO. A three-dimensional schematic is established to elucidate the role of ZnO in the CeO_2 – Gd_2O_3 system.

© 2012 Elsevier B.V. All rights reserved.

1. Introduction

Over the past decades, significant efforts have been exerted to reducing the operating temperatures of solid oxide fuel cells [1–3]. Operation at the low and intermediate temperatures (below 800 °C) can effectively alleviate the phase reaction between the cell components and enable the use of low-cost metallic materials (such as stainless steel) as interconnect materials [4–7]. Doped ceria, especially gadolinia-doped ceria (GDC), has been regarded as

one of the most promising candidate electrolytes for intermediate temperature solid oxide fuel cells [8–10]. The main drawback of GDC is the increased electronic conductivity under reducing conditions, but this effect becomes negligible when operating below 600 °C [11].

At low and intermediate temperatures, the grain-boundary (GB) resistivity dominates the overall resistivity of GDC. The blocking effect of GB originates from various contributions. The grain-to-grain contacts act as “intrinsic” charge barriers in nature, which has been successfully explained by the space-charge effect [12–14]. In the space-charge model, an “effective” GB consists of a core and two adjacent space-charge layers. Structurally, the space-charge layers are parts of the bulk near the GB. The GB core of GDC is

* Corresponding author. Tel.: +86 25 83587261; fax: +86 (0)25 83306152.

E-mail address: lc-guo@163.com (L. Guo).

suggested to be positively charged; thus, the oxygen vacancies are depleted in the space-charge layers and the GB exerts a blocking effect [12,15]. On the other hand, the segregation of impurities is widely reported as the “extrinsic” origin of the highly resistive GB [8,13,16–18]. The “intrinsic” blocking effect becomes insignificant at elevated temperatures (e.g., $>600\text{ }^{\circ}\text{C}$) [19]. By contrast, the “extrinsic” blocking effect caused by the segregation of impurities dominates the overall resistivity up to $1000\text{ }^{\circ}\text{C}$ [20]. SiO_2 is regarded as one of the most ubiquitous impurities present in GDC, along with some alkali metal oxides (e.g., CaO_2). These impurities accumulate at GBs and form amorphous intergranular siliceous phases, which can wet along the GB during sintering and markedly increase the GB resistance. Unfortunately, SiO_2 is prone to be included during powder preparation, ceramic formation, and sintering [13,16,17,20]. Hence, the scavenging of the harmful siliceous phase is essential even for relatively pure materials.

Our group [21] has found that ZnO doping can effectively increase the GB conductivity of doped ceria. A unique “island structure” can be observed on the ZnO-added GDC surface, which is clearly distinguished from the clean surface of pristine GDC after applying the same sintering treatment. Energy dispersive X-ray spectroscopy (EDS) analysis reveals that the “floating” particles contain high levels of Si and Gd elements [21]. The segregation of Si is speculated to be responsible for the improved GB conductivity. However, cases of ZnO-added samples with clean surfaces also show improved GB conductivities after sintering at a low temperature. The mechanism of the siliceous phase segregation is still unclear.

In this paper, the scavenging effect of ZnO doping on 2000 ppm SiO_2 in GDC is reported. The mechanism of this effect was studied by AC impedance spectroscopy and transmission electron microscopy (TEM) combined with energy-dispersive X-ray spectroscopy (EDS).

2. Experimental Section

2.1. Sample preparation

Powders of $\text{Ce}_{0.8}\text{Gd}_{0.2}\text{O}_{1.9}$ (GDC) were first prepared from commercial CeO_2 (99.5%; Yixing Xinwei Leeshing Rare Earth Co., China) and Gd_2O_3 (99.99%; Beijing Founde Star Science and Technology Co., China) powders. Stoichiometric quantities of the GDC powders were mechanically mixed with 2000 ppm SiO_2 (99.95%; Shanghai Chemical Reagent Plant, China) and 0–5 mol% ZnO (99.95%; Shanghai Chemical Reagent Plant, China) by ball milling. The powders were then uniaxially die pressed at 100 MPa into cylindrical pellets, and sintered in air at $1400\text{ }^{\circ}\text{C}$ for 10 h, some pellets were annealed at the same temperature for 20 h for heat-treatment. Given the refractory nature of the specimens without ZnO doping, they were sintered at $1600\text{ }^{\circ}\text{C}$ for 10 h. The heating rate was $100\text{ }^{\circ}\text{C h}^{-1}$, and the specimens were slowly air cooled after sintering. The sintered specimens doped with x mol% ZnO are denoted as $\text{GDCSi-}x\text{Zn}$. For example, a specimen labeled “ GDCSi-1Zn ” is 1 mol% ZnO-doped $\text{Ce}_{0.8}\text{Gd}_{0.2}\text{O}_{1.9}$ containing 2000 ppm SiO_2 .

2.2. Characterization

The relative densities of the sintered samples were determined by Archimedes’ principle. The crystalline phase of the specimens (ground to powder for measurement) at room temperature was identified using an X-ray diffractometer (XRD, ARL-X’TRA, Thermo, USA) with $\text{Cu K}\alpha$ radiation at 40 kV and 35 mA. The scanning electron microscopy (SEM) studies were performed using a JEOL JSM-6360 equipment. The average grain sizes were measured from the SEM images and estimated using the JEOL SMileView software.

The microstructures near the GB were observed using a transmission electron microscope (TEM, Tecnai F20, FEI, USA) with an energy dispersive X-ray spectroscopy instrument. Specimens for TEM analysis were prepared by ultrasonic cutting, mechanical thinning, polishing, dimpling, and Ar-ion milling using a Gatan Duo-mill (Gatan, Warrendale, PA, USA) at 0.5 mA and 4 kV.

The oxide ionic conductivity of the sintered pellets was measured by AC impedance spectroscopy in air from $200\text{ }^{\circ}\text{C}$ to $500\text{ }^{\circ}\text{C}$ within 0.1 Hz–100 kHz using an impedance analyzer (PARSTAT 2273). Silver paste was painted on both sides of the pellets and fired at $700\text{ }^{\circ}\text{C}$ for 10 min to ensure good bonding before measurement. Curve fitting and resistance calculations were performed using ZSimpWin software.

3. Results and discussion

3.1. Synthesis characterization

Fig. 1 shows the XRD patterns of the specimens. All samples consisted of a single fluorite phase (CeO_2 , Fm3m). No significant second phase was found in GDCSi , GDCSi-0.5Zn , and GDCSi-1Zn (Fig. 1a–c). The ionic size of Zn^{2+} ($0.090\text{ }\text{\AA}$) at a coordination number of 8 is smaller than those of Gd^{3+} ($1.06\text{ }\text{\AA}$) and Ce^{4+} ions ($0.97\text{ }\text{\AA}$). In our previous studies [22,23], the solid solubility limit of Zn in CeO_2 is found to be quite low ($\sim 0.6\text{ mol\%}$). The solid solubility limit explains the slight ZnO peaks identified in GDCSi-2Zn and GDCSi-5Zn . For the same reason, the addition of ZnO causes only a minor perturbation in the lattice parameters (Supplementary Materials, Figure S1).

Table 1 shows the specification, composition, sintering temperature, relative density, and average grain size of the sintered samples. Given the sintering-aid effect of ZnO [21–23], the relative density of $\text{GDCSi-}x\text{Zn}$ (sintered at $1400\text{ }^{\circ}\text{C}$) was comparable to that of GDCSi (sintered at $1600\text{ }^{\circ}\text{C}$). Fig. 2 shows the SEM photographs of the surfaces of the sintered samples. No obvious second phase was found on the surfaces of the samples, or the amount of the second phase was below the detection limit of the EDS equipment. By contrast, as a result of post-sintering heat treatment, the samples show unique “island structures” (Supplementary Materials, Figure S2), which is consistent with our previous contribution [21]. Naturally, the samples sintered at $1600\text{ }^{\circ}\text{C}$ have larger grain sizes. Notably, GDC and GDCSi show comparable d_g values, indicating that Si addition does not harm grain growth and

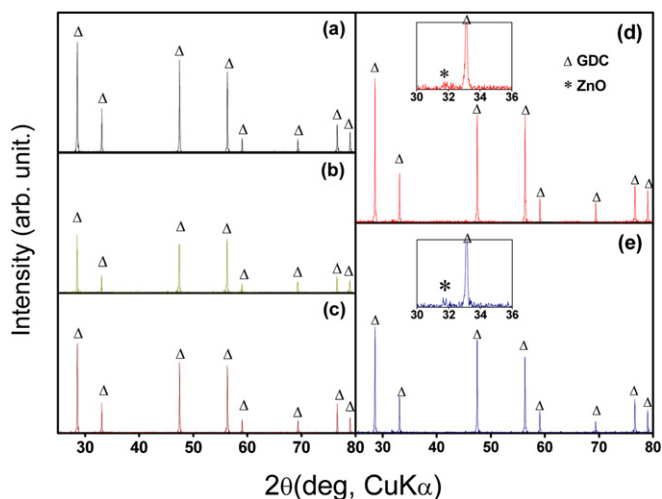


Fig. 1. XRD patterns of (a) GDCSi , (b) GDCSi-0.5Zn , (c) GDCSi-1Zn , (d) GDCSi-2Zn , and (e) GDCSi-5Zn .

Table 1

Specifications, sintering temperatures, densities, and average grain sizes of the samples all sintered for 10 h.

Samples	Composition	Sintering T (°C)	Relative density (%)	d_g ^a (μm)
GDC	20GDC	1600	95.4	4.45
GDCSi	20GDC + 2000 ppm SiO ₂ ^b	1600	95.5	4.41
GDCSi–0.5Zn	20GDC + 2000 ppm SiO ₂ +0.5 mol% ZnO	1400	84.4	0.80
GDCSi–1Zn	20GDC + 2000 ppm SiO ₂ + 1 mol% ZnO	1400	94.6	1.39
GDCSi–2Zn	20GDC + 2000 ppm SiO ₂ + 2 mol% ZnO	1400	95.3	1.71
GDCSi–5Zn	20GDC + 2000 ppm SiO ₂ + 5 mol% ZnO	1400	95.0	1.81

^a Average grain size measured by the SMileView (Ver. 2.1) software.

^b By weight percentage.

densification. A high SiO₂ content reportedly has a remarkable effect on the densification and grain growth of Ce_{1-x}Gd_xO_{2- δ} [24]. This effect is found to be positive when $x < 0.2$ and negative when $x > 0.2$.

On the other hand, for GDCSi– x Zn, d_g increases with increased ZnO concentration. According to a previous report [21], the addition of ZnO can increase mass transport and promote grain growth. However, under the same sintering conditions, the reported d_g of GDC–1Zn (3.05 μm) [21] is much higher than that of GDCSi– x Zn (0.80–1.81 μm). This observation indicated that grain growth was suppressed when SiO₂ and ZnO were added together, although ZnO has been proven to be an effective grain-growth promoter when added alone.

3.2. Electrochemical impedance spectroscopy (EIS) analysis

Fig. 3 shows the complex impedance spectra of specimens obtained at 350 °C. Generally, at low temperatures, the impedance plots consisted of three arcs that correspond to the contribution of the grain interior, GB, and electrode, respectively. The

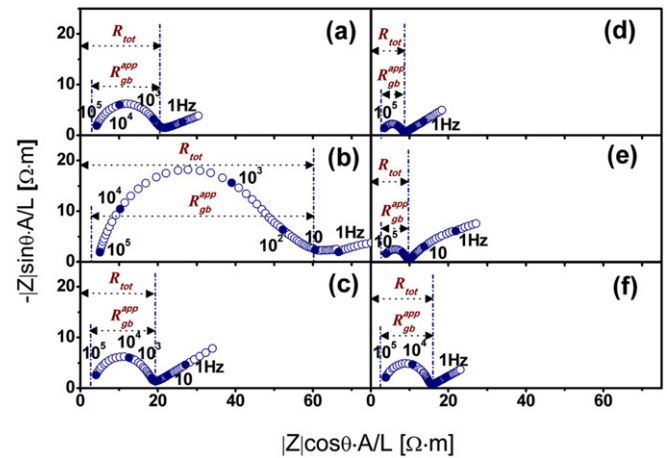


Fig. 3. Complex impedance spectra of (a) GDC, (b) GDCSi, (c) GDCSi–0.5Zn, (d) GDCSi–1Zn, (e) GDCSi–2Zn, and (f) GDCSi–5Zn at 350 °C in air.

specimens exhibited a typical spectrum with two arcs; the first arc represents the GB contribution for which the capacitance lies in the nF range [25,26]. The grain interior arc was not well resolved because of the limited frequency range used in this work (0.1 Hz–100 kHz).

The contribution of the grain interior and GB can be clearly distinguished in the impedance spectra up to 500 °C. Hence, the resistance of the GB can be accurately calculated within 200–450 °C. The impedance spectra were curve fitted with an $R(QR)(QR)$ equivalent circuit, where R is the resistance and Q is the pseudo-capacitance. The grain interior resistance of the electrolyte is given by

$$R_{gi} = R_{tot} - R_{gb}^{app} \quad (1)$$

Fig. 4 shows the values of the grain interior resistivity (R_{gi}), apparent GB resistivity (R_{gb}^{app}), and total resistivity (R_{tot}) as

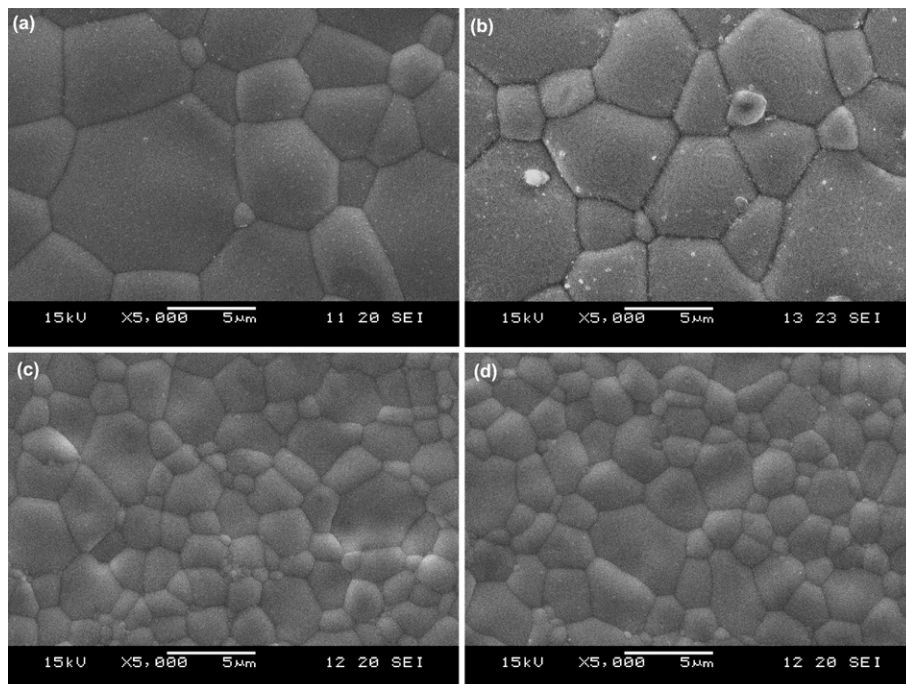


Fig. 2. Scanning electron micrographs of (a) GDC, (b) GDCSi (20GDC + 2000 ppm SiO₂), (c) GDCSi–1Zn (GDCSi + 1 mol% ZnO), (d) GDCSi–5Zn (GDCSi + 5 mol% ZnO).

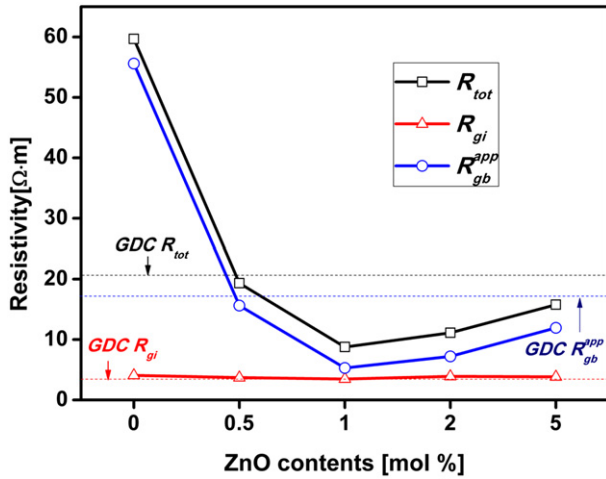


Fig. 4. Grain interior, apparent grain boundary, and total resistivities of GDCSi with different ZnO contents measured at 350 °C.

a function of the ZnO doping concentrations. The resistivity values of pristine GDC are also plotted in dotted lines for comparison. Fig. 4 shows that the R_{gi} values of GDCSi doped with and without ZnO had only minor perturbation. The R_{gi} values were similar at 3.4–3.9 Ω m. The grain interior behavior of GDC was almost unaffected by the additives (SiO_2 or ZnO) used in this experiment. This finding agreed with our previous reports [21,22]. By contrast, the R_{gb}^{app} values showed obvious variation. The R_{gb}^{app} of pristine GDC was 17.19 Ω m, whereas that of GDCSi was 55.59 Ω m. This significant increase can be attributed to the addition of SiO_2 . Given the rapid diffusion of siliceous impurity along the GB, even a trace amount of SiO_2 was significantly detrimental to the GB conduction. With the addition of ZnO, the R_{gb}^{app} values remarkably decreased. Fig. 4 shows that the R_{gb}^{app} of GDCSi-xZn decreased with increased x until $x = 1$, and then increased with further addition. GDCSi-1Zn showed the minimum value of R_{gb}^{app} (5.19 Ω m), which was only about one-eleventh that of GDCSi. Notably, the R_{gb}^{app} arcs of GDCSi-1Zn, GDCSi-2Zn, and GDCSi-5Zn (Fig. 3d–f) were smaller than those of GDC (Fig. 3a). This would be mainly due to the deleterious effect of the SiO_2 contained in GDC (~ 200 ppm) [21].

R_{gb}^{app} was used to obtain the apparent GB conductivity (σ_{gb}^{app}) from the equation

$$\sigma_{gb}^{app} = \frac{1}{R_{gb}} \times \frac{L}{A} = \frac{1}{R_{gb}^{app}} \quad (2)$$

where L is the separation of the electrodes (usually the sample thickness) and A is the electrode area. The series values of σ_{gb}^{app} calculated from Eq. (2) with R_{gb}^{app} is shown in Fig. 5 in the form of $\ln(\sigma_{gb}^{app} \cdot T)$.

However, σ_{gb}^{app} was calculated with R_{gb} and the macroscopic dimension of the specimen (L/A). Thus, σ_{gb}^{app} depended on the grain sizes because the number of GBs governs ion transport. Hence, the specific GB conductivity (σ_{gb}^{sp}) should be estimated to remove the effects of grain sizes.

According to the brick-layer model, σ_{gb}^{sp} can be calculated from the average grain size d_g and average GB thickness δ_{gb} . This model was proposed by Van Dijk and Burggraaf [27], which assumes that the GB of the ceramic sample consists of a continuous and uniform layer with higher resistivity than grains. In the brick-layer model, the following approximations with respect to the microstructure are required: (i) cubic-shaped grains with equal sizes of d_g , and (ii)

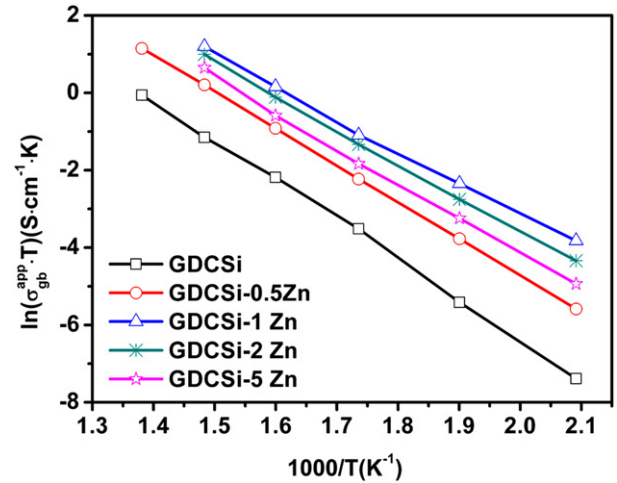


Fig. 5. Arrhenius plot of the apparent grain boundary conductivity for GDCSi-xZn.

homogeneous GBs of thickness δ_{gb} (where $\delta_{gb} \ll d_g$). Thus, the specific GB conductivity (σ_{gb}^{sp}) is defined by the equation [8,16,28]

$$\sigma_{gb}^{sp} = \sigma_{gb}^{app} \frac{\delta_{gb}}{d_g} = \frac{1}{R_{gb}^{app}} \times \frac{\delta_{gb}}{d_g} \quad (3)$$

The precise determination of δ_{gb} is difficult. Fortunately, the GB thickness lies in a fairly narrow range (1–2 nm) for all sintered samples [29]. Hence, the changes in σ_{gb}^{sp} can be related to those in $1/(R_{gb}^{app} \cdot d_g)$. In previous studies, the same approximate computation has been carried out to assess the specific GB behaviors of polycrystalline samples [8,30].

The calculated results shown in Fig. 6 suggested that σ_{gb}^{sp} of the ZnO-added samples were much higher than that of GDCSi. Thus, ZnO-doping can effectively alleviate the deleterious effect of the siliceous intergranular phase. GDCSi-1Zn also showed the maximum σ_{gb}^{sp} over the entire temperature range tested. According to results measured at 350 °C, the addition of 1 mol% ZnO increased the σ_{gb}^{sp} of GDCSi up to about 35 times. As an n-type semiconductor, the addition of ZnO may contribute to the total conductivity to some degree. However, the blocking effect of the ZnO phase on oxygen-ion transport led to decreased GDCSi-xZn conductivity with increased x , as shown in Figs. 5 and 6.

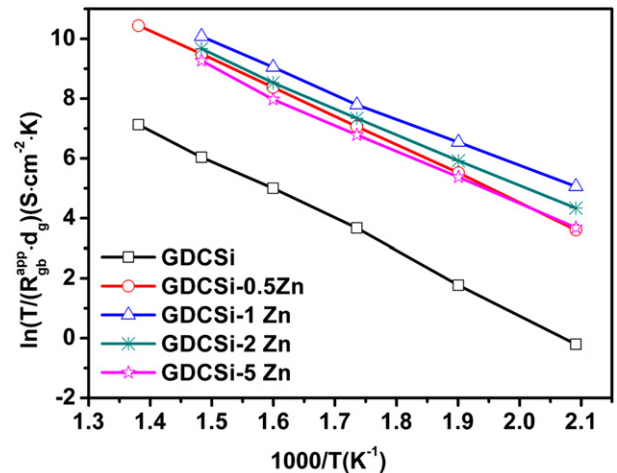


Fig. 6. Alternative representation of the specific grain boundary conductivity taking into account the average grain sizes of GDCSi-xZn.

3.3. FETEM-EDS analysis

To understand the changes in GB behavior, high-resolution TEM (HRTEM) was used to observe the GB of GDCSi and GDCSi–1Zn (Figs. 7 and 8). The corresponding EDS results of the specific areas of the specimens are shown. As expected, siliceous phases were frequently found at the triple grain junctions of GDCSi (Fig. 7a). On the other hand, GDCSi–1Zn exhibited clean triple grain junctions (Fig. 8a). Surprisingly, two kinds of intergranular phase in small quantities were observed in GDCSi–1Zn. The EDS result (Fig. 8f) suggested that the second phase marked in Fig. 8d was rich in Zn. This finding was reasonable because the solubility limit of ZnO in GDC is quite low according to our previous studies [22,23]. More importantly, Fig. 8c shows the aggregation of a siliceous intergranular phase. EDS results showed high levels of Gd and Si, small amounts of Ce and Ca, as well as trace amounts of ZnO (less than 1 at.%). This finding indicated that ZnO induced the strong aggregation of the siliceous intergranular phases, consistent with the improved GB conductivity of GDCSi–xZn.

Fig. 9 shows the HRTEM images of the GBs of GDCSi and GDCSi–1Zn. The GB of GDCSi–1Zn was almost free of any siliceous second phase, different from that of GDCSi. The morphology of the intergranular siliceous phase has been summarized in two models [19]. One model assumes that the intergranular siliceous phase

forms a continuous film coating on the grains, but such a situation is unlikely to be observed in real materials. The other model considers grains to be partly coated by the siliceous phases; the coverage depends on many factors, particularly the wetting properties of the siliceous phase. In this experiment, the siliceous phases were located between two grains in GDCSi (Fig. 9a). However, determining the continuity of the morphology of the siliceous phase was difficult.

$\text{FeO}_{1.5}$, CaO, and SrO reportedly have beneficial effects on the GB conduction of Si-containing GDC [24,27,31,32]. However, research on the reaction mechanisms of Si-containing GDC is limited. Recently, MgO and BaO are found to be effective scavenger materials, and their scavenging mechanisms are respectively attributed to the formation of Mg_2SiO_4 and $\text{Ba}_2\text{Si}_3\text{O}_8$ based on microstructural analysis by complementary techniques such as TEM, electron energy-loss spectroscopy, and electron probe microanalysis [18,33]. In the well-established stabilized zirconia system, the scavenging mechanism of Al_2O_3 on the siliceous phase is also related to the formation of mullite ($\text{Al}_6\text{Si}_2\text{O}_{13}$). However, the presence of zinc silicates (e.g., Zn_2SiO_4) in the specimens has not been proven. Although some uncertainties exist because of the sectioning problem, the strong aggregation of the nearly Zn-independent siliceous phase (Fig. 8c) suggests a new mechanism in which the scavenging of the siliceous phase does not occur via the formation of zinc silicates.

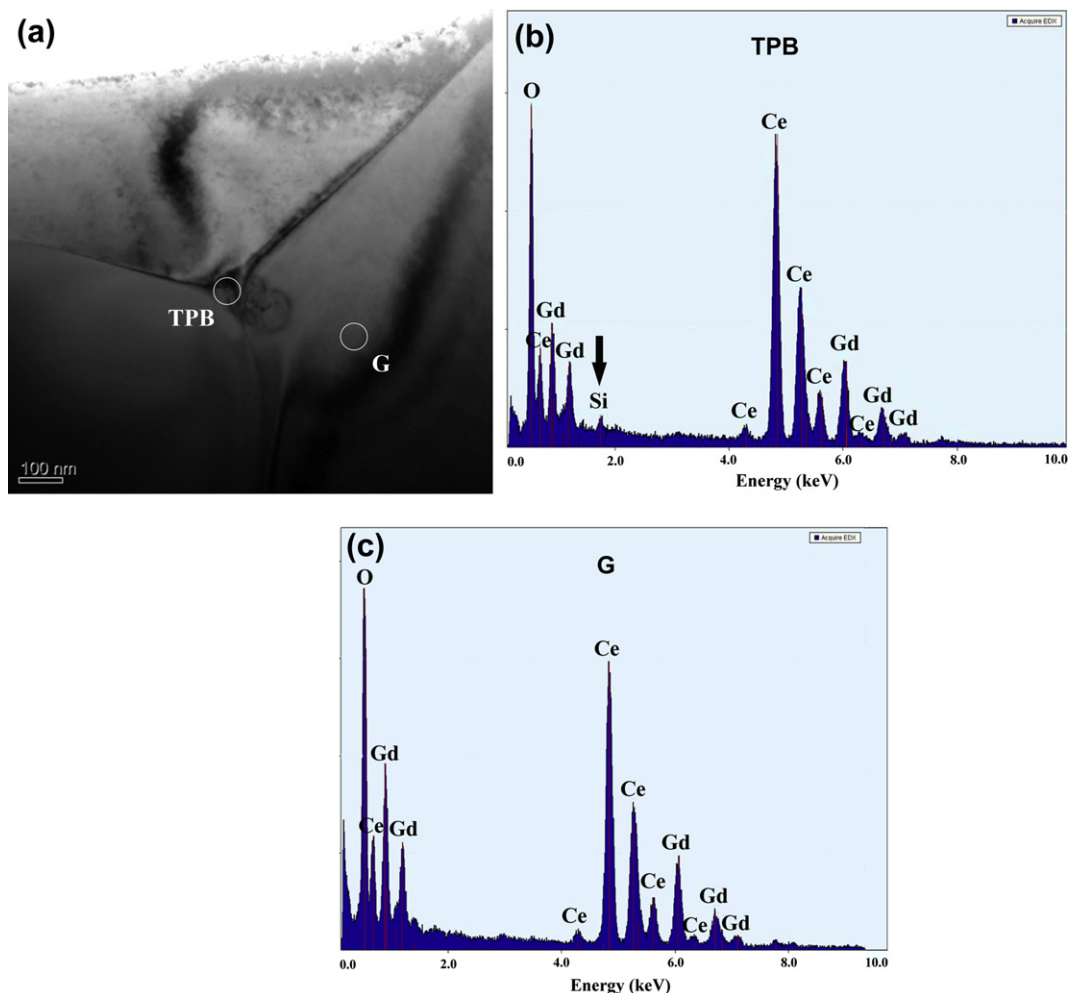


Fig. 7. (a) TEM image of GDCSi specimen and EDS spectra at the (b) triple boundary (TPB) and (c) grain interior (G).

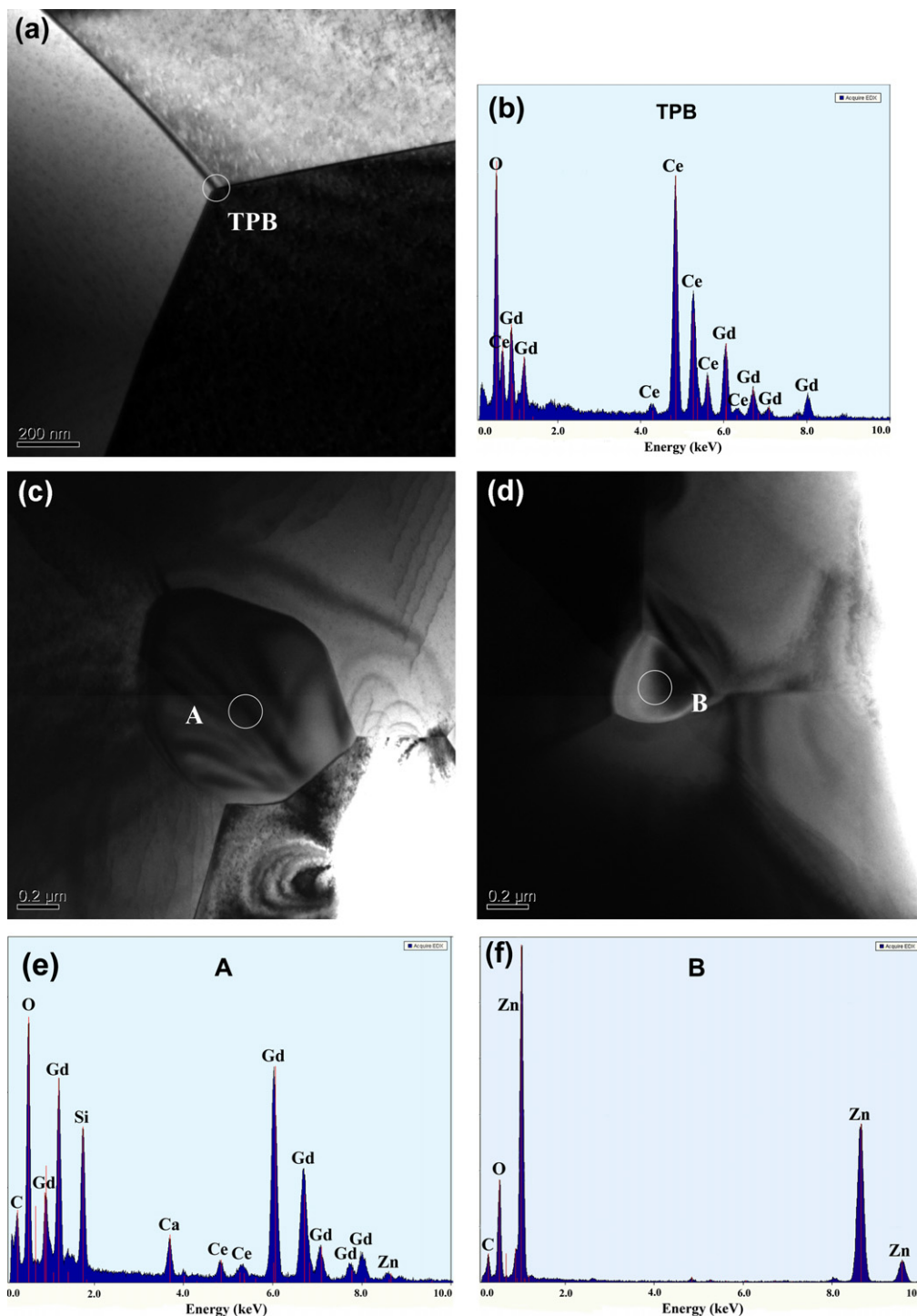


Fig. 8. (a) TEM image of a triple boundary in GDCSi–1Zn; (b) EDS spectrum at the triple boundary (TPB); TEM images of the (c) siliceous phases and (d) zinc-rich phase; and the corresponding EDS spectra at the locations indicated in (e) siliceous phase (marked as A) and (f) zinc-rich phase (marked as B).

As aforementioned, the wetting behavior determines the distribution status of the intergranular siliceous phase and the current constriction near the GB. A comparison of the morphologies of the siliceous phases in Figs. 7 and 8c revealed that the dihedral angle of the liquid phase significantly increased with ZnO addition. Another significant change was the strong aggregation of the siliceous phase in the ZnO-added specimen with diameter of $\sim 0.8 \mu\text{m}$. According to Kingery [34], the dihedral angle ϕ depends on the relationship between the interfacial and GB energies:

$$\cos \frac{\phi}{2} = \frac{1}{2} \frac{\gamma_g}{\gamma_{SL}} \quad (4)$$

where γ_g and γ_{SL} are the GB energy and solid–liquid interface energy, respectively. When ϕ is less than 60° , the second phase is suggested to be permeable and the liquid penetration along the GBs is dominant. Thus, for GDCSi, the penetration of the siliceous phase along the grain boundaries is normally represented by low dihedral angles (Fig. 7a). Conversely, when ϕ is greater than 120° , the

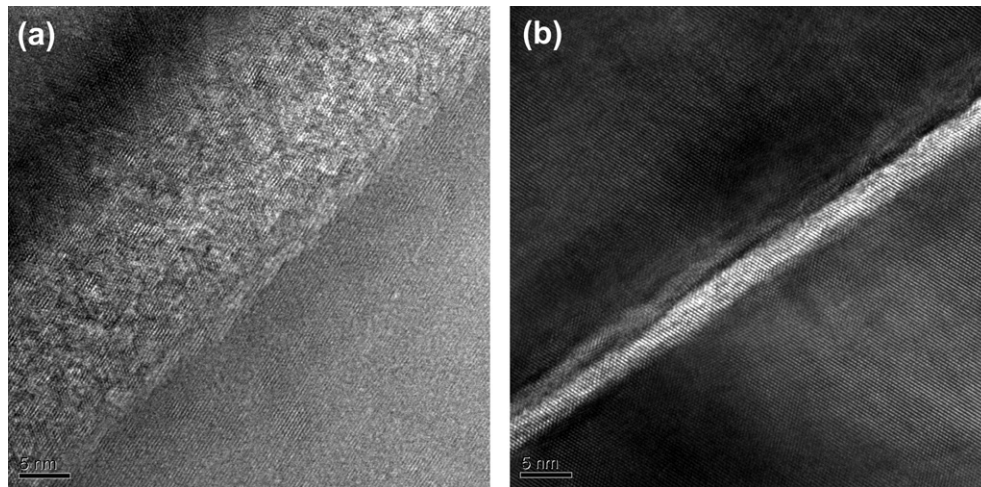


Fig. 9. HRTEM photographs of the grain boundary of (a) GDCSi and (b) GDCSi–1Zn.

interfacial energy γ_{SL} is greater than the GB energy and the second phase forms isolated pockets at grain intersections. Thus, penetration along the GBs becomes impossible. Fig. 8c shows that the dihedral angle was almost 180° and the aggregated siliceous phase showed a completely non-wetting behavior.

Our previous contribution [21] reveals that particles containing high levels of Si and Gd emerge on the surfaces of ZnO-doped GDC after high temperature thermal etching. This phenomenon was also observed in the present experiment (Figure S2, Supplementary Materials). The composition of the “floating” particles was also almost completely identical with the siliceous phase aggregated between grains (Fig. 8e). Hence, the gathered siliceous pockets produced by ZnO addition dynamically migrated by grain growth and densification during high-temperature thermal etching. Therefore, the “floating” particles were expected to be the crystallized form of the intergranular liquid siliceous phase expelled from the interior. Considering that the etching temperature was

much lower than the melting point of ZnO (1975°C), the ZnO phase did not migrate to the specimen surface, as expected.

Fig. 10 illustrates the three-dimensional (3D) microstructure of the specimens. Fig. 10a shows the permeable nature of the siliceous phase. Siliceous impurity was diffused along the GB and coated or partly coated the grains, which led to high GB resistivity. For specimens with ZnO added, ZnO and a siliceous phase were observed to be separately aggregated at the triple junction areas, as shown in Fig. 10b. The Zn- and Si-rich second phases in GDCSi–xZn were impermeable, which explained the higher GB conduction of the GDCSi–xZn specimens than GDCSi. The strong aggregation of the non-wetting siliceous phase indicated that ZnO addition may modify the viscosity and wettability of the siliceous phase by the dissolution of trace amounts of ZnO. During the thermal etching procedure, the liquid siliceous phases were expelled onto the surface because of densification and grain growth, as shown in Fig. 10c. The siliceous phases were also crystallized during the cooling process, and the specimens consequently demonstrated the unique “island structure”.

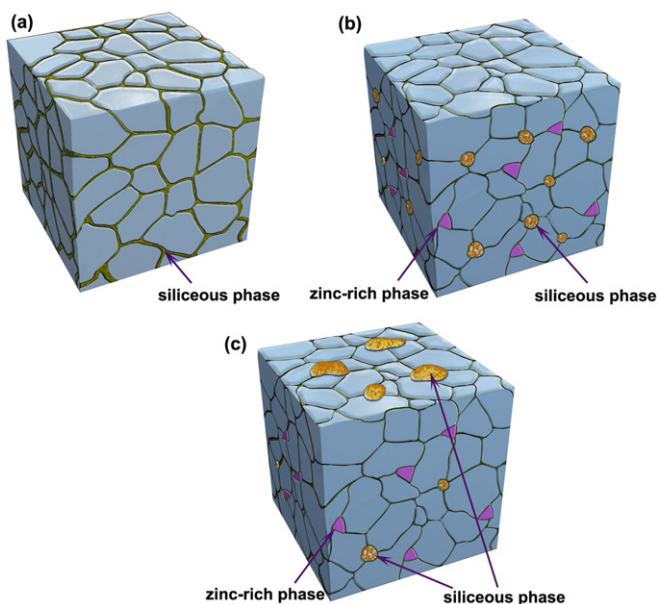


Fig. 10. Schematic of the sintered samples (a) GDCSi, (b) GDCSi–xZn, and (c) GDCSi–xZn after post-sintering heat treatment.

4. Conclusions

The effect of ZnO addition on the GB behavior of GDCSi was investigated. The specific GB conduction of GDCSi was enhanced up to 35 times by the addition of 1 mol% ZnO. TEM combined with EDS revealed that siliceous phases became strongly aggregated in non-wetting configurations after ZnO addition. The deleterious effect of siliceous phases was not mitigated by the formation of zinc silicates (e.g. Zn_2SiO_4) but by a new mechanism in which ZnO merely accelerated the aggregation of intergranular siliceous phases.

Acknowledgments

This work was financially supported by the Priority Academic Program Development (PAPD) of Jiangsu Higher Education Institutions, the Graduate Science and Technology Innovation Foundation of Jiangsu (CXZZ11_0324), and Program for Changjiang Scholars and Innovative Research Team in University (PCSIRT), IRT1146. We are deeply grateful to Yan Liu, Guoxin Chen, and Huifeng Chen at the Ningbo Institute of Material Technology and Engineering of the Chinese Academy of Sciences for their assistance with the HRTEM and EDS analyses.

Appendix A. Supplementary data

Supplementary data related to this article can be found at <http://dx.doi.org/10.1016/j.jpowsour.2012.12.084>.

References

- [1] R.M. Ormerod, Chem. Soc. Rev. 32 (2003) 17–28.
- [2] Z. Shao, S.M. Haile, Nature 431 (2004) 170–173.
- [3] B.C.H. Steele, A. Heinzel, Nature 414 (2001) 345–352.
- [4] Z. Shao, W. Zhou, Z. Zhu, Prog. Mater. Sci. 57 (2012) 804–874.
- [5] M.H. Sossina, Acta Mater. 51 (2003) 5981–6000.
- [6] T. Suzuki, Z. Hasan, Y. Funahashi, T. Yamaguchi, Y. Fujishiro, M. Awano, Science 325 (2009) 852–855.
- [7] D.J.L. Brett, A. Atkinson, N.P. Brandon, S.J. Skinner, Chem. Soc. Rev. 37 (2008) 1568–1578.
- [8] G.M. Christie, F.P.F. van Berkel, Solid State Ionics 83 (1996) 17–27.
- [9] J.L.M. Rupp, A. Infortuna, L.J. Gauckler, Acta Mater. 54 (2006) 1721–1730.
- [10] M. Morales, J.J. Roa, X.G. Capdevila, M. Segarra, S. Piñol, Acta Mater. 58 (2010) 2504–2509.
- [11] M.G. Bellino, D.G. Lamas, N.E. Walsøe de Reca, Adv. Funct. Mater. 16 (2006) 107–113.
- [12] X. Guo, R. Waser, Prog. Mater. Sci. 51 (2006) 151–210.
- [13] X. Guo, W. Sigle, J. Maier, J. Am. Ceram. Soc. 86 (2003) 77–87.
- [14] S. Kim, J. Maier, J. Electrochem. Soc. 149 (2002) J73–J83.
- [15] W. Lee, H.J. Jung, M.H. Lee, Y.-B. Kim, J.S. Park, R. Sinclair, F.B. Prinz, Adv. Funct. Mater. 22 (2012) 965–971.
- [16] C. Tian, S.-W. Chan, Solid State Ionics 134 (2000) 89–102.
- [17] P.-S. Cho, S.B. Lee, Y.H. Cho, D.-Y. Kim, H.-M. Park, J.-H. Lee, J. Power Sources 183 (2008) 518–523.
- [18] Y.H. Cho, P.-S. Cho, G. Auchterlonie, D.K. Kim, J.-H. Lee, D.-Y. Kim, H.-M. Park, J. Drennan, Acta Mater. 55 (2007) 4807–4815.
- [19] X.-D. Zhou, W. Huebner, I. Kosacki, H.U. Anderson, J. Am. Ceram. Soc. 85 (2002) 1757–1762.
- [20] B.C.H. Steele, Solid State Ionics 129 (2000) 95–110.
- [21] L. Ge, S. Li, Y. Zheng, M. Zhou, H. Chen, L. Guo, J. Power Sources 196 (2011) 6131–6137.
- [22] L. Gao, M. Zhou, Y. Zheng, H. Gu, H. Chen, L. Guo, J. Power Sources 195 (2010) 3130–3134.
- [23] S. Li, L. Ge, H. Gu, Y. Zheng, H. Chen, L. Guo, J. Alloys Compd. 509 (2011) 94–98.
- [24] T.S. Zhang, J. Ma, S.H. Chan, P. Hing, J.A. Kilner, Solid State Sci. 6 (2004) 565–572.
- [25] R. Gerhard, A.S. Nowick, J. Am. Ceram. Soc. 69 (1986) 641–646.
- [26] J.T.S. Irvine, D.C. Sinclair, A.R. West, Adv. Mater. 2 (1990) 132–138.
- [27] T. van Dijk, A.J. Burggraaf, Physica Status Solidi Aa 63 (1981) 229–240.
- [28] S. Hui, J. Roller, S. Yick, X. Zhang, C. Decès-Petit, Y. Xie, R. Maric, D. Ghosh, J. Power Sources 172 (2007) 493–502.
- [29] D. Pérez-Coll, D. Marrero-López, P. Núñez, S. Piñol, J.R. Frade, Electrochim. Acta 51 (2006) 6463–6469.
- [30] M. Mogensen, N.M. Sammes, G.A. Tompsett, Solid State Ionics 129 (2000) 63–94.
- [31] T.S. Zhang, J. Ma, L.B. Kong, S.H. Chan, P. Hing, J.A. Kilner, Solid State Ionics 167 (2004) 203–207.
- [32] J.A. Lane, J.L. Neff, G.M. Christie, Solid State Ionics 177 (2006) 1911–1915.
- [33] S.-Y. Park, P.-S. Cho, S.B. Lee, H.-M. Park, J.-H. Lee, J. Electrochem. Soc. 156 (2009) B891–B896.
- [34] W.D. Kingery, H.K. Bowen, D.R. Uhlmann, Introduction to Ceramics, second ed., Wiley, New York, 1976.